Bryn Mawr College

Scholarship, Research, and Creative Work at Bryn Mawr College

Geology Faculty Research and Scholarship

Geology

2010

Seasonal H2O and CO2 Ice Cycles at the Mars Phoenix Landing Site: 1. Prelanding CRISM and HiRISE Observations

Selby Cull
Bryn Mawr College, scull@brynmawr.edu

Raymond E. Arvidson

Michael Mellon

Sandra Wiseman

Roger Clark

See next page for additional authors

Custom Citation

Cull, S., R. E. Arvidson, M. Mellon, S. Wiseman, R. Clark, T. Titus, R. V. Morris, and P. McGuire (2010), Seasonal H2O and CO2 ice cycles at the Mars Phoenix landing site: 1. Prelanding CRISM and HiRISE observations, *J. Geophys. Res.*, 115, E00D16, doi: 10.1029/2009JE003340.

Authors

Selby Cull, Raymond E. Arvidson, Michael Mellon, Sandra Wiseman, Roger Clark, Timothy Titus, Richard V. Morris, and Patrick McGuire

Seasonal H$_2$O and CO$_2$ ice cycles at the Mars Phoenix landing site: 1. Prelanding CRISM and HiRISE observations

Selby Cull,[1] Raymond E. Arvidson,[1] Michael Mellon,[2] Sandra Wiseman,[1] Roger Clark,[3] Timothy Titus,[4] Richard V. Morris,[5] and Patrick McGuire[6]

[1] The condensation, evolution, and sublimation of seasonal water and carbon dioxide ices were characterized at the Mars Phoenix landing site from Martian northern midsummer to midspring (L$_s$ ~ 142° – L$_s$ ~ 60°) for the year prior to the Phoenix landing on 25 May 2008. Ice relative abundances and grain sizes were estimated using data from the Compact Reconnaissance Imaging Spectrometer for Mars and High Resolution Imaging Science Experiment aboard Mars Reconnaissance Orbiter and a nonlinear mixing model. Water ice first appeared at the Phoenix landing site during the afternoon in late summer (L$_s$ ~ 167°) as an optically thin layer on top of soil. CO$_2$ ice appeared after the fall equinox. By late winter (L$_s$ ~ 344°), the site was covered by relatively pure CO$_2$ ice (~30 cm thick), with a small amount of ~100 μm diameter water ice and soil. As spring progressed, CO$_2$ ice grain sizes gradually decreased, a change interpreted to result from granulation during sublimation losses. The combined effect of CO$_2$ sublimation and decreasing H$_2$O ice grain sizes allowed H$_2$O ice to dominate spectra during the spring and significantly brightened the surface. CO$_2$ ice disappeared by early spring (L$_s$ ~ 34°) and H$_2$O ice by midspring (L$_s$ ~ 59°). Spring defrosting was not uniform and occurred more rapidly over the centers of polygons and geomorphic units with relatively higher thermal inertia values.

1. Introduction

[2] NASA's Phoenix Scout mission landed on the northern plains of Mars on 25 May 2008, at solar longitude (L$_s$) ~80°, at 68.22°N, 125.70°W (planetocentric) [*Smith et al.*, 2009]. Mission science objectives focused on characterizing the high-latitude environment and implications for habitability, including mapping subsurface ice and tracking seasonal polar changes from northern late spring through summer [*Smith et al.*, 2008].

[3] The Phoenix landing site is within the area covered by the seasonal ice cap, a layer of CO$_2$ and H$_2$O ice that extends down to 50°N and covers the permanent northern H$_2$O ice cap from late summer through late spring [*Larson and Fink*, 1972; *James et al.*, 1993]. More than 25% of the carbon dioxide in the Martian atmosphere condenses to form the seasonal cap, beginning in late northern summer and coinciding with the onset of regional dust storms in the southern hemisphere [*Forget et al.*, 1995; *Kieffer and Titus*, 2001]. Atmospheric dust may act as condensation nuclei for seasonal CO$_2$ ice, although the majority of CO$_2$ ice is expected to form directly on the surface as a result of radiative cooling [*Forget et al.*, 1998]. Estimates of CO$_2$ ice depth and duration within the Phoenix latitude band (65°–72°N) vary considerably; however, at the pole, the cap grows to more than a meter deep by midwinter [*Smith et al.*, 2001], and begins to sublimate during early spring, finally disappearing by late spring [*Wagstaff et al.*, 2008]. As the CO$_2$ ice sublimates, it leaves behind an annulus of water ice [*Bibring et al.*, 2005], perhaps deposited in fall and reexposed during the spring, or cold trapped onto the surface during or after CO$_2$ sublimation [*Seelos et al.*, 2008]. The large spatial scale, volume of CO$_2$, and the global dust, CO$_2$, and H$_2$O cycle dynamics make the seasonal evolution of the polar cap one of the more important climatic processes on Mars.

[4] The CO$_2$ cap is relevant to the Phoenix mission because it is closely tied to the presence and dynamics of ground H$_2$O ice. Shallow groundwater ice fills in subsurface

[1]Department of Earth and Planetary Sciences, Washington University in Saint Louis, Saint Louis, Missouri, USA.
[2]Laboratory for Atmospheric and Space Physics, University of Colorado at Boulder, Boulder, Colorado, USA.
[3]U.S. Geological Survey, Denver, Colorado, USA.
[4]U.S. Geological Survey, Flagstaff, Arizona, USA.
[5]ARES, NASA Johnson Space Center, Houston, Texas, USA.
[6]Institute for Geosciences, Freie Universitaet Berlin, Berlin, Germany.

soil pore spaces and increases thermal conductivity, which allows more summer heat into the ground [*Mellon et al.*, 2008a]. Gradually released, this heat warms the surface enough to slow the CO_2 ice rate of condensation and to increase the rate of sublimation [*Aharonson*, 2004; *Kieffer*, 2007; *Haberle et al.*, 2008]. The depth to the top of the ground ice is in turn controlled by surface soil properties and albedo variations [*Sizemore and Mellon*, 2006], both of which influence ice deposition and sublimation rates.

[5] Because the seasonal CO_2 cap is a major component of the ice and dust cycles and is closely related to ground-water ice, it is important to understand its behavior at the Phoenix landing site. Previous studies have characterized the large-scale behavior of the seasonal cap and shown that the cap deposition and retreat patterns are longitude-dependent, especially at midlatitudes [*James and Cantor*, 2001; *Benson and James*, 2005]. There is considerable disagreement among data sets examined prior to this study on the cap evolution within the Phoenix latitude band. In particular, the reported "crocus date," or date of the disappearance of the last CO_2 ice [*Titus et al.*, 2001], varies widely: from $L_s \sim 35°–55°$ based on Thermal Emission Spectrometer (TES) temperature estimates [*Kieffer and Titus*, 2001], to $L_s \sim 70°$ based on models from High-Energy Neutron Detector (HEND) data [*Litvak et al.*, 2005]. In MOC images, the edge of the cap reached $\sim 68°N$ by $L_s \sim 44°$ during the 2000 recession, and by $L_s \sim 48°$ during the 2002 recession [*Benson and James*, 2005]. Viking Infrared Thermal Mapper data shows the cap edge reaching $\sim 68°N$ at $L_s \sim 56°$ [*James and Cantor*, 2001].

[6] The Phoenix primary and extended mission lasted most of the Martian northern summer ($L_s \sim 80°$ to $145°$) [*Smith et al.*, 2009; *Arvidson et al.*, 2009]. However, our understanding of ice and dust cycles at the landing site is incomplete without analyses of ice evolution from $L_s \sim 145°$ to $L_s \sim 80°$ (late summer, fall, winter, and spring). In this paper, detailed analyses are presented of the winter-to-spring and summer-to-fall evolution of ice around the Phoenix landing site, using high-resolution orbital data. The data cover $65°N–72°N$, $230°E–250°E$ ("region D" in *Seelos et al.* [2008]), an area that was selected for the Phoenix landing site for its low rock abundances and postulated shallow groundwater ice [*Arvidson et al.*, 2008; *Mellon et al.*, 2008a].

[7] The prelanding advance and retreat of ices over the Phoenix site discussed in this paper were observed using hyperspectral data from the Compact Reconnaissance Imaging Spectrometer for Mars (CRISM) [*Murchie et al.*, 2007] onboard Mars Reconnaissance Orbiter (MRO). To estimate changes in ice grain sizes and abundances, non-linear mixing models [*Hapke*, 1981, 1993] were used to calculate reflectances of theoretical soil-H_2O-CO_2 mixtures. Images from the MRO High Resolution Imaging Science Experiment (HiRISE) [*McEwen et al.*, 2007] were used to track small-scale sublimation patterns in spring, and to estimate changing ice thicknesses. CRISM and color HiRISE images were also used to track changes in surface brightness and color. These analyses, when combined with coordinated Phoenix ground and orbital observations, will provide a full year view of the surface ice and dust cycles at the landing site.

2. Spectral Fitting: Data Sets and Methods

[8] The CRISM instrument consists of two detectors: a shortwave ("S") detector with bands between 0.3646 and 1.0560 μm, and a long-wavelength ("L") detector with bands between 1.0014 and 3.9368 μm. The spectrometer is mounted to a gimbal platform, which enables off-nadir pointing and ground tracking of a target. CRISM can operate either in hyperspectral (544 channels) or multi-channel (72 channel subset) mode. In multispectral mode, the gimbal is pointed to nadir and remains fixed, collecting 10 km wide observations at 72 wavelengths and either 100 or 200 m/pixel resolution. In hyperspectral, or targeted mode, the gimbal scans along the optical line of sight, allowing for longer integration times without along-track smear. Targeted observations are taken with all 544 wavelengths, at either full spatial resolution (FRT; 15–19 m/pixel) or 2x spatially binned (HRS/HRL; 30–40 m/pixel) to cover a larger area. CRISM data utilized in this study were processed to units of *I/F* (spectral radiance at the sensor divided by solar spectral irradiance divided by pi).

[9] This study used 49 FRTs taken over "region D," most of which were taken in the summer and spring (Figure 1), with a few observations acquired in fall and winter. All but three of the observations were acquired between 1330–1500 local mean solar time (LMST).

2.1. Atmospheric Correction

[10] CRISM *I/F* spectra have radiative contributions from both the surface and atmosphere, including gas and aerosol absorption, scattering, and emission. This study uses the Discrete Ordinate Radiative Transfer (DISORT) model [*Stamnes et al.*, 1988; *Wolff et al.*, 2007] to separate atmospheric and surface contributions from CRISM *I/F* spectra. DISORT can be used to calculate (1) the scattering and attenuation of a solar beam down through the atmosphere, (2) interactions with a user-defined surface, and (3) scattering and attenuation up through the atmosphere. We used routines with DISORT that are optimized for calculations of the Martian atmosphere [*Wolff et al.*, 2009] and procedures developed for use with CRISM data [*Arvidson et al.*, 2008; *Wiseman*, 2009]. DISORT was used to generate a series of modeled *I/F* spectra that would be observed at the top of the atmosphere (e.g., contain both surface and atmospheric contributions) given known surface reflectance spectra. The DISORT model results were used to retrieve surface reflectance values (e.g., atmospherically corrected spectra) from measured CRISM *I/F* data using a lookup table approach. This process is diagrammed in Figure 2.

[11] For this process to accurately atmospherically correct CRISM spectra, we must accurately approximate the atmosphere at the time of observation (section 2.1.1) and the scattering behavior of the surface (section 2.1.2).

2.1.1. Defining Atmospheric Parameters

[12] We included in our model the atmospheric pressure-temperature profile, contributions from atmospheric gases (CO_2, CO, H_2O), and contributions from aerosols (dust and ice). Temperatures for each layer of the atmosphere were taken from historical Thermal Emission Spectrometer (TES) climatology observations at the appropriate latitude, longitude, and L_s [*Conrath et al.*, 2000; *Smith*, 2002]. Surface pressure was based on Viking Lander measurements, and
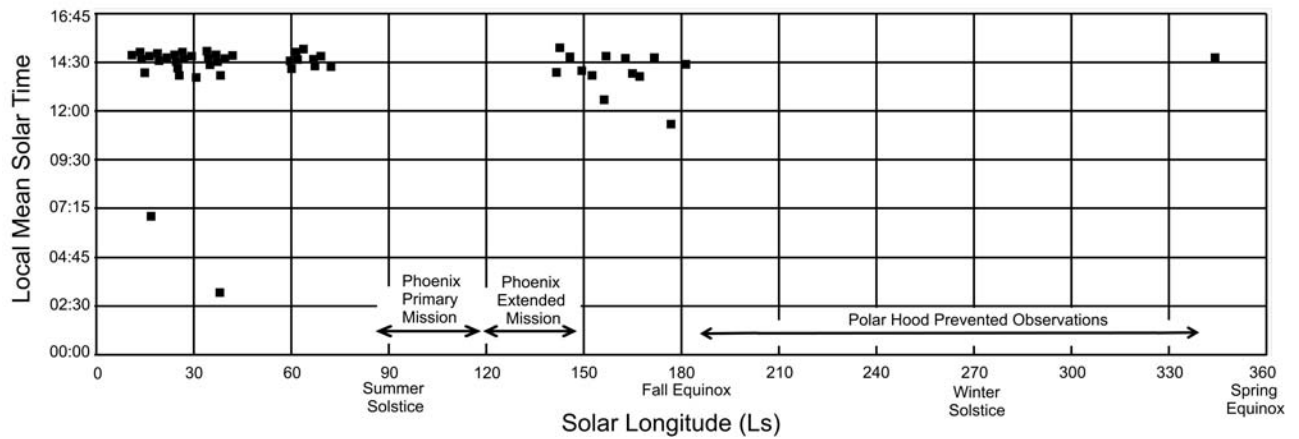
Figure 1. CRISM FRT coverage over solar longitude (L_s) and local mean solar time (LMST). With only three exceptions, all of the FRTs used in this study were acquired between 1330–1500 LMST. Most of the observations were acquired during spring ($L_s \sim 0°–90°$) or late summer ($L_s \sim 90°–180°$).

the pressure for each atmospheric layer calculated by integrating the hydrostatic equilibrium equation [*Conrath et al.*, 2000]. H_2O vapor abundances were taken from historical TES data [*Smith*, 2002]. Dust and ice aerosol abundances were also derived from historical TES estimates of the optical depth (tau) of dust at 9.3 μm and ice at 12.1 μm [*Smith*, 2004].

[13] To account for aerosol scattering effects, ice and dust single-scattering albedos (w) and particle phase functions [$p(g)$] were input and radiatively modeled. For ice, w was calculated using optical constants from *Warren* [1984] and an assumed particle radius of 2.0 μm, and $p(g)$ was modeled as a Legendre polynomial with coefficients from *Clancy et al.* [2003]. For dust, w was calculated using optical constants derived from CRISM observations [*Wolff et al.*, 2009] and an assumed particle radius of 1.5 μm, and $p(g)$ was modeled as a wavelength-dependent Legendre polynomial with coefficients from *Wolff et al.* [2009]. Dust aerosols were assumed to be uniformly distributed throughout each layer, with a constant volume-mixing ratio, and ice aerosols were assumed to be well mixed above the altitude at which water condenses.

[14] To account for small (<∼1 nm) time-dependent shifts in center wavelength due to instrument temperature changes, radiative transfer models were first run with high spectral resolution (0.1 nm spacing) over the CO_2 gas band region, and the wavelengths resampled and fit to observed wavelengths to determine wavelength offset, a technique developed by *Wiseman et al.* [2007] and *Wiseman* [2009].

2.1.2. Defining the Surface

[15] The lower boundary of the atmosphere was defined within DISORT as a surface that scatters light according to the scattering model [*Hapke*, 1993]:

$$r(i,e,g) = \frac{w}{4\pi} \frac{\mu_0}{\mu_0 + \mu} \{[1 + B(g)]p(g) + H(\mu_0)H(\mu) - 1\} \quad (1)$$

where i, e, and g are the incidence, emergence, and phase angles, respectively; $r(i,e,g,)$ is the bidirectional reflectance observed, μ_0 is the cosine of i, μ is the cosine of e, $B(g)$ is the opposition effect, $p(g)$ is the surface phase function, and $H(\mu_0)$ $H(\mu)$ describe multiple scattering.

[16] The surface phase function was modeled as a two-lobed Henyey-Greenstein model [*Henyey and Greenstein*, 1941]:

$$p(g) = \frac{(1 - \delta^2)f}{(1 - 2\delta \cos(g) + \delta^2)^{3/2}} + \frac{(1 - \delta^2)(1 - f)}{(1 + 2\delta \cos(g) + \delta^2)^{3/2}} \quad (2)$$

where f is a weighting factor that describes the scattering direction ($f = 0$ for forward scatter, $f = 1$ for backscatter) and δ is an asymmetry factor constrained to be between -1 and 1 ($\delta = 0$ for isotropic scatter).

[17] Deriving the spectrophotometric functions for Phoenix soils and ices is beyond the scope of this paper; however, it is important to constrain them to reasonable values, since scattering parameter selection can affect the overall albedo of a spectrum (Figure 3). *Cull et al.* [2010] showed that surface soils at the Phoenix landing site have scattering parameters similar to those derived by *Johnson et al.* [2006] for soils at the Spirit landing site at Gusev Crater: an asymmetry parameter of 0.498, forward-scattering fraction of 0.817, and h of 0.385. The Gusev Crater Soil endmember is a widespread plains unit photometrically similar to many Martian soils, including soils at the Viking 1 [*Arvidson et al.*, 1989] and Mars Pathfinder landing sites [*Johnson et al.*, 1999]. We assumed soils at the Phoenix landing site have the same scattering properties as Gusev soils.

[18] The opposition effect, $B(g)$, was ignored in our calculations, because it is only important for observations with small phase angles. FRTs used in this study were obtained with large phase angles (>40°).

2.1.3. Retrieval of Surface Reflectance From CRISM I/F

[19] In order to calculate atmospherically corrected surface reflectance from CRISM I/F, DISORT was used to model the I/F that would be observed at the top of the atmosphere for 6 input surfaces with variable w values, with all other parameters fixed. The relationship between modeled I/F and calculated w was determined using a fifth-order polynomial fit to output from DISORT calculations. For each CRISM band, a look-up table between modeled I/F and w was used to retrieve w for a measured

CRISM *I/F* value (Figure 2). Atmospheric parameters were adjusted slightly and the models rerun to remove residual atmospheric contributions, if necessary. Examples of pre-atmospherically and postatmospherically corrected spectra are shown in Figure 4.
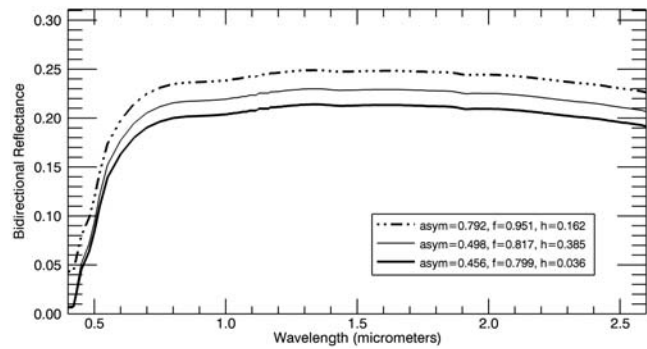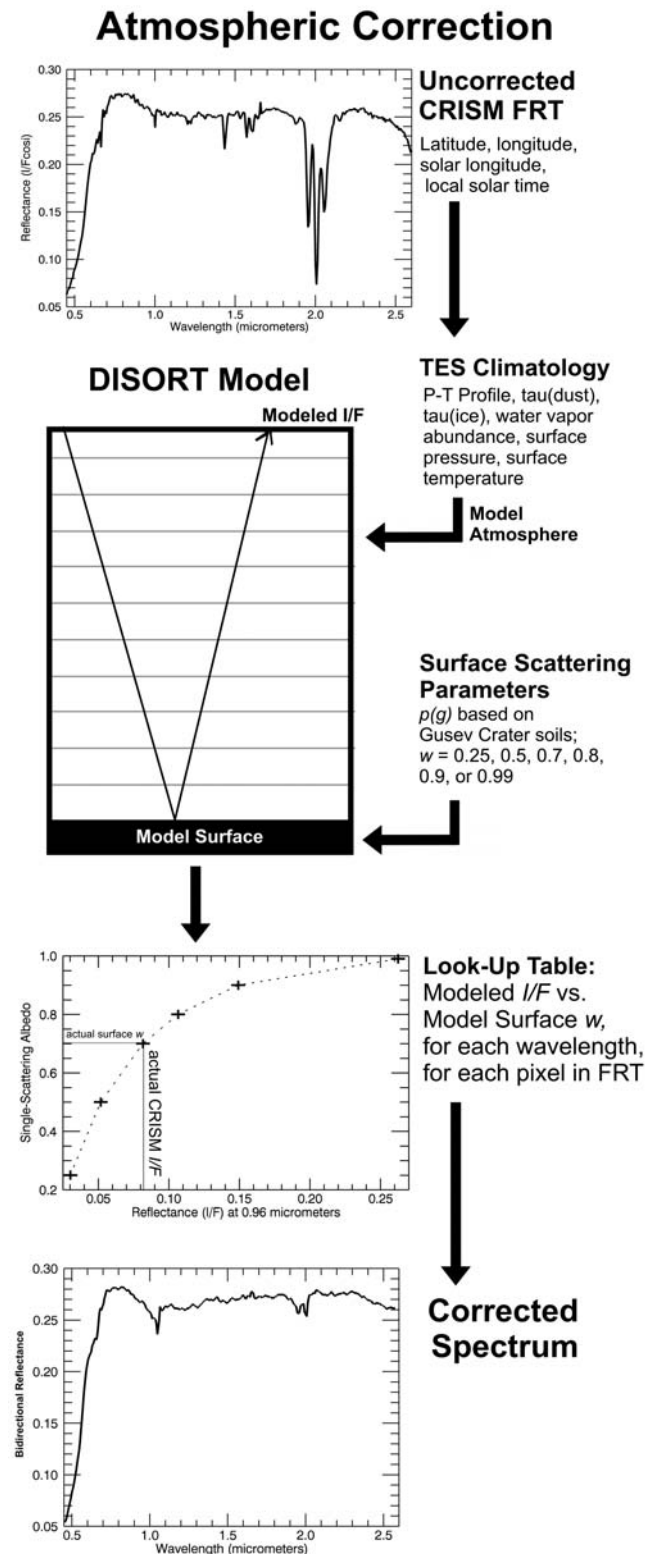
Atmospheric Correction

Uncorrected CRISM FRT
Latitude, longitude, solar longitude, local solar time

DISORT Model
Modeled I/F

TES Climatology
P-T Profile, tau(dust), tau(ice), water vapor abundance, surface pressure, surface temperature

Model Atmosphere

Surface Scattering Parameters
p(g) based on Gusev Crater soils; *w* = 0.25, 0.5, 0.7, 0.8, 0.9, or 0.99

Model Surface

Look-Up Table:
Modeled *I/F* vs. Model Surface *w*, for each wavelength, for each pixel in FRT

Corrected Spectrum

Figure 2. The atmospheric correction process for CRISM FRTs. On the basis of each observation's latitude, longitude, and time of observation, historical TES climatology data were used to estimate atmospheric conditions at the time of observation, including a pressure-temperature profile, ice and dust optical depths, and water vapor abundances. This atmospheric profile was used in a DISORT model, along with surface-scattering parameters based on Gusev Crater soils, to calculate the radiance at the top of the atmosphere for each CRISM wavelength. Six DISORTs were run for each cube, varying the surface single-scattering albedo, and a look-up table created to relate single-scattering albedo to *I/F*.

Figure 3. Model results of 10 μm diameter palagonite with varying surface scattering parameters. The scattering parameters were derived from various materials at the Gusev Crater landing site by *Johnson et al.* [2006] and are (top line) sol 102–103 gray rock end-member, (middle line) sol 212–225 soil end-member, and (bottom line), sol 212–225 red rock end-member.

[20] Because subsequent surface modeling (see section 2.2.1) was done in terms of bidirectional reflectance, retrieved values of *w* as a function of wavelength were converted to bidirectional reflectance using equation (1).

2.2. Modeling of Surface Spectra

[21] To estimate the relative abundances and grain sizes of H_2O ice, CO_2 ice, and soil in CRISM observations, spectra of theoretical mixtures of these three components were generated using a nonlinear mixing model, and compared to bidirectional surface reflectance spectra retrieved from CRISM images as described in section 2.1.

2.2.1. Spectral Mixing Model

[22] CRISM bidirectional surface reflectance spectra were extracted from the geomorphic unit on which Phoenix landed: the unit first named lowland bright by *Seelos et al.* [2008] and later renamed Heimdal outer ejecta by *Heet et al.* [2009]. This unit is widespread around the Phoenix landing site and visible in CRISM observations acquired at multiple L_s. Five-by-five pixel average spectra were compared across the unit in each scene and a representative spectrum selected for modeling.

[23] To extract grain sizes and relative abundances of water ice, CO_2 ice, and soil, each spectrum was modeled using the nonlinear mixing model described by *Hapke*
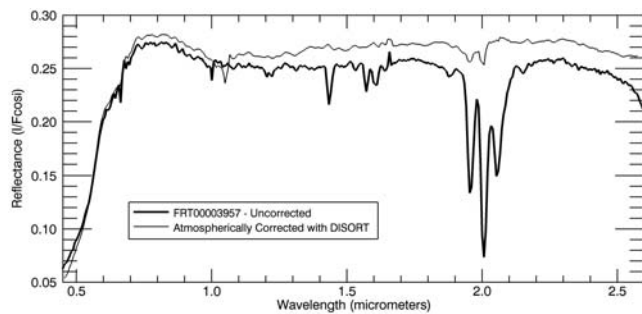
Figure 4. Comparison of DISORT-corrected CRISM spectrum (thin line) and original, uncorrected spectrum (thick line). The small hashes in the corrected spectrum are due to residual CO_2 gas from the correction.

[1981, 1993]. Single-scattering albedos of mixtures were calculated as from *Hapke* [1981]:

$$w = \frac{\sum_{i=1}^{i=n} (Q_{Si} M_i / \rho_i D_i)}{\sum_{i=1}^{i=n} (Q_{Ei} M_i / \rho_i D_i)} \qquad (3)$$

where M_i is the mass fraction of component i, ρ_i the solid density, D_i the diameter, Q_{Si} the scattering efficiency, Q_{Ei} the extinction efficiency, and the summation is carried out for all components in the mixture. Because the particles considered here are large compared to the wavelengths, we assume that the extinction efficiency is 1, which indicates that the particle's surface is affecting the entire wavefront [*Hapke*, 1981]. The scattering efficiency is calculated using the internal and external reflection coefficients and the absorption coefficient, as described in detail by *Roush* [1994]. In addition, to account for observations with a layer of transparent ice covering soil, a two-layer nonlinear mixing model described by equations (9.31a–e) in *Hapke* [1993] was used. For each spectrum, $p(g)$ parameters were matched to the DISORT parameters discussed in section 2.1.2. Because the size parameter ($X = \pi D / \lambda$) is $\gg 1$ for our wavelength region, we ignore the effects of resonant oscillations.

[24] In the layered models, the thickness of the overlying layer was calculated based on the cross-sectional mass (e.g., mg/cm^2). To convert this to a layer thickness, the cross-sectional mass was divided by the material's solid density.

[25] In our nonlinear mixing models, we ignored the effects of macroscale roughness, since the Hapke model's roughness term [e.g., *Hapke*, 1984] appears to be inaccurate for high-albedo surfaces [*Byrne et al.*, 2008; *Domingue et al.*, 1997], and macroscale roughness should not be a significant factor at the Phoenix landing site, where slopes are typically $\leq 5°$ [*Kirk et al.*, 2008]. With these assumptions, the bidirectional reflectance of the surface depended on material properties (optical constants, particle size, and density) and observational geometry (i, e, g, and λ). In our modeling, we used CRISM wavelengths and FRT-specific incidence, emergence, and phase angles.

[26] Three surface components were included in the nonlinear modeling: H_2O ice, CO_2 ice, and a Mars soil analog. The soil component utilized optical constants based on a Mauna Kea palagonite sample: a low-temperature alteration product of fine-grained basaltic ash [*Clancy et al.*, 1995]. Based on both orbital and ground observations, dehydrated palagonite mixed with nanophase iron oxides appears to be a good analog for the Phoenix site soils [*Arvidson et al.*, 2009; *Heet et al.*, 2009]. For modeling, optical constants were used from *Hansen* [1997, 2005] for CO_2 ice, *Warren* [1984] for H_2O ice, and solid densities of $\rho = 1.562$ g/cm^3 for solid CO_2, $\rho = 0.9167$ g/cm^3 for solid H_2O, and $\rho = 2.700$ g/cm^3 for palagonite were assumed. The bidirectional reflectance was then modeled as a function of grain size and relative mass fraction. We define "grain size" as a grain's diameter.

[27] Water ice and soil optical constants were resampled to the band passes used in the CO_2 optical constants measurements, because their absorption features are less likely to be altered by resampling than the narrow CO_2 ice absorptions. Bidirectional reflectances were calculated with the Hapke model, and the results were convolved to CRISM band passes [*Murchie et al.*, 2007].

2.2.2. Sensitivity Analysis

[28] For each spectrum, initial best fit parameters were obtained by inspection and a chi-square (X^2) value calculated:

$$\chi^2 = \sum_{\lambda=1}^{n} \frac{(r_o - r_m)^2}{r_o^2} \qquad (4)$$

where r_o is the observed bidirectional reflectance, r_m is the modeled bidirectional reflectance, and the summation was carried out over all wavelengths (except between 1.95 μm and 2.1 μm, an area sometimes disrupted by residual CO_2 gas bands in DISORT-derived spectra).

[29] Because these models include multiple variables, multiple sets of parameters can produce low X^2 values. We therefore consider the initial best fit set of parameters a local minimum in X^2 space. To test for the existence of other local minima, we performed a sensitivity analysis: one parameter was fixed while the others were allowed to vary and a new X^2 was calculated; then, the fixed parameter was increased to a higher or lower fixed value, and the others allowed to vary, and so on until the parameter had been assigned each of its physically reasonable values. This process resulted in X^2 as a function of the fixed parameter, as illustrated in Table 1. For each spectrum, this process was carried out for each parameter (grain size, mass ratio, or upper layer thickness), and local minima identified. Of the local minima identified, some could be discarded because the depths of the major absorptions did not match. Some could be discarded because of physical constraints (for example, the thickness of the overlying layer could not be less than the diameter of the particles that made it up). After discarding the parameter sets that were physically unreasonable and those that produced band depths that were too shallow or too deep, only one set of parameters was left for most FRTs. Some FRTs (FRT0000939A, FRT000093F5, FRT0000A07E) had multiple sets of parameters; these were discarded as being too poorly constrained. Only those with a single set of best fit parameters are analyzed here.

[30] We further tested each best fit set of parameters to determine which variables within each fit were well constrained and which were poorly constrained. To do this, one

Table 1. Example of a Sensitivity Analysis for FRT0000419C Shown for a Subset of One Parameter[a]

Upper Layer					Lower Layer				Results	
Soil Grain Size (μm)	Water Ice Grain Size (μm)	Soil Mass Fraction	Water Ice Mass Fraction	Upper Layer Thickness	Soil Grain Size (mm)	Water Ice Grain Size (μm)	Soil Mass Fraction	Water Ice Mass Fraction	Chi-Squared	1.5 μm Band Depth
1	80	0.1	0.9	1.3	3	0	1	0	0.214	0.071
5	70	0.1	0.9	3.1	3	0	1	0	0.152	0.161
10	80	0.3	0.7	3.3	2	0	1	0	0.205	0.132
15	70	0.5	0.5	3.1	2	0	1	0	0.041	0.097
20	80	0.7	0.3	4.2	3	0	1	0	0.283	0.073
30	100	0.8	0.2	5.5	2	0	1	0	0.073	0.066
50	60	0.4	0.6	6.1	2	0	1	0	0.119	0.140
100	50	0.7	0.3	6.9	3	0	1	0	0.295	0.131
150	70	0.5	0.5	7.1	3	0	1	0	0.402	0.207
250	50	0.4	0.6	6.8	3	0	1	0	0.176	0.165

[a]For each run, the fixed parameter (in this case, soil grain size of the upper layer) was held constant and the other variables allowed to adjust until a best fit for that grain size was found, then that grain size was increased incrementally. The lowest chi-square value for this example occurred for soil grain sizes of 15 μm, a combination of parameters that also produced a 1.5 μm band depth (0.097) comparable to the actual 1.5 μm band depth for FRT0000419C (0.095). Soil grain size of 30 μm also produced a low chi-square value (0.073); however, that set of parameters produced too small of a 1.5 μm band depth (0.066), and so was not considered a good solution.

variable was varied in steps away from its original value and the fitting process repeated for each step. If the variable was well constrained, the chi-square value increased quickly as the value moved away from the best fit value (e.g., Figure 9e). For poorly constrained variables, chi-square values increased slowly away from the best fit. Sensitivity analysis results are presented in section 3.4.

3. Spectral Fitting Results

3.1. Summer to Fall

[31] Representative summer and early fall CRISM spectra are plotted in Figure 5. As previously reported by *Seelos et al.* [2008], Phoenix ice-free summer spectra show a ferric edge in the VNIR, indicating contributions from nanophase iron oxides, and a reflectance dropoff starting at 2.3 μm, which is typical of the northern plains and has been interpreted as small amounts of water adsorbed onto the surface [e.g., *Jouglet et al.*, 2007; *Milliken et al.*, 2007]. Ice-free summer spectra were best modeled as a thin layer (~95 μm thick) of 15 μm soil overlying coarser-grained soil (~2 mm), based on use of the palagonite optical constants. This result is not inconsistent with Phoenix Optical Microscope (OM) and Robotic Arm Camera (RAC) results, which indicate an abundance of translucent reddish grains of silt to sand sizes, appearing in undisturbed state as aggregates of larger particles [*Arvidson et al.*, 2009; *Pike et al.*, 2009].

[32] CRISM data show water ice forming near the Phoenix landing site in late summer, with 1.5 and 2 μm bands appearing by L_s ~167° (Figure 5). The late summer spectra were best fit by a 1:1 ice:soil layer of 50 μm H_2O ice with 15 μm soil particles over sand-sized particles (2 mm), consistent with dirty ice overlying soil deposits ($X^2 = 0.354$). The thickness of the icy layer increases from ~90 μm to ~113 μm from L_s ~167° to L_s ~177°, but the grain sizes and ice:soil ratio stay the same.

3.2. Winter

[33] CRISM obtained only one winter spectrum (L_s ~344°) due to the presence of the polar hood. This spectrum is dominated by CO_2 ice (Figure 6). The 2 μm triplet is saturated, as are the 1.43 and 2.12 μm bands. The 1.2 μm doublet

and 1.87, 2.283, 2.34 μm bands - all of which are only present in CO_2 ice, not in the gas phase - are all strong. There are also shallow H_2O ice absorptions, including a broad 1.5 μm band, a broadening at 2.0 μm beyond what would be expected of CO_2 ice, and the 2.3 μm turndown.

[34] Atmospheric corrections were run on this observation; however, because the observation's high incidence
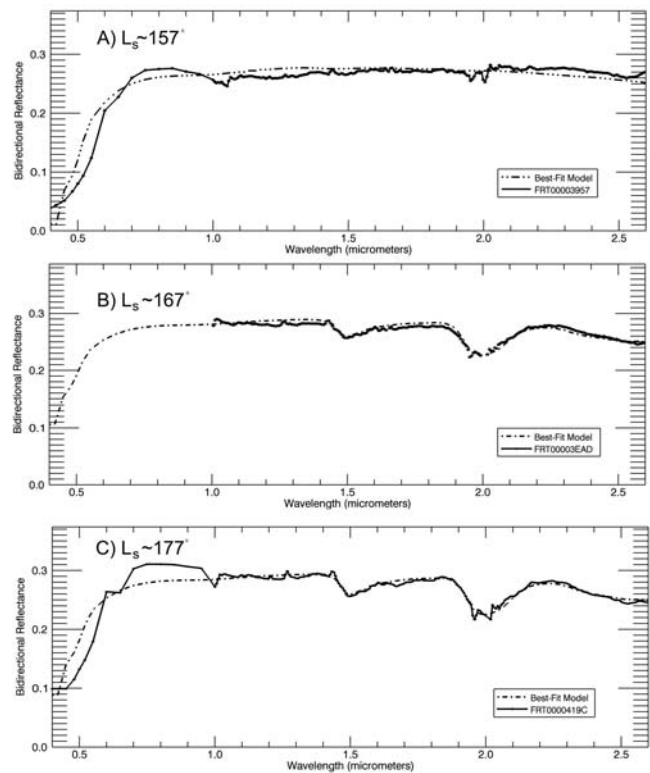

Figure 5. Late summer spectra over the Phoenix landing site. (a) No ice has yet formed. (b) The 1.5 μm and 2.0 μm absorptions illustrate that water ice has begun to condense. (c) The 1.5 μm and 2.0 μm absorptions become stronger. Model parameters for these observations are given in Table 2.
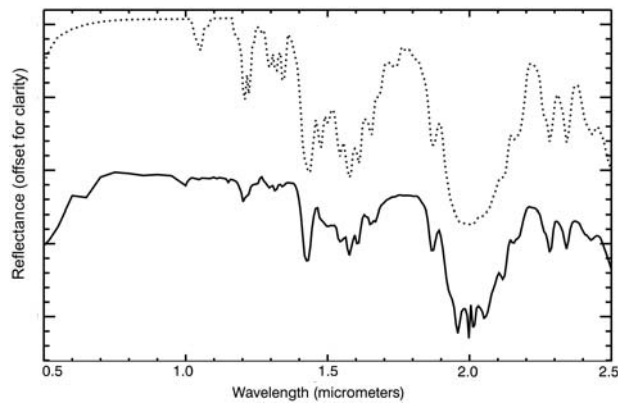
Figure 6. Winter CRISM observation over Phoenix landing site (solid curve) and model results (dotted curve). DISORT corrections have removed most of the observation's CO_2 gas bands, but, due to the observation's high incidence angle, it was not possible to calculate absolute bidirectional reflectances for this observation.

angle (81.3° relative to the areoid) violated the DISORT assumption that the atmosphere behaves as series of plane parallel layers, absolute bidirectional reflectances could not be obtained. The observation could not be accurately modeled using the nonlinear mixing model. However, information on grain sizes and abundances could still be extracted from the spectrum using only the absorption band depths.

[35] CO_2 ice grain sizes were estimated by comparing the depth of the 2.283 μm ice-only absorption in the observation (37.7%) to band depths modeled using the nonlinear mixing model. The 2.283 μm CO_2 ice band depth best matched models of CO_2 ice with "grain sizes" of 30 cm. (At this scale, the CO_2 can be thought of as a solid slab with long light path lengths, rather than individual grains.) Water ice grain sizes were estimated by comparing the 1.5 μm band depth in the observation (24.7%) and the slope between 2.2 and 2.5 μm to models, and best matched models with a layer of 100 μm grain size water ice overlying the CO_2 slab (Figure 6).

3.3. Spring

[36] The earliest springtime CRISM FRT was taken 72 sols after the winter observation, at L_s ~11°, and the spectrum is quite different than the winter spectrum (Figure 7a). H_2O ice absorptions at 1.5 and 2.0 μm dominate, and the 2.3–2.6 region is steeply negative, corresponding to coarser-grained H_2O ice (~100 μm). CO_2 ice absorptions are still apparent at 1.43, 2.28, and 2.34 μm. The overall reflectance is higher than observed in spectra acquired during the winter: rising to a bidirectional reflectance of ~0.5 at L_s ~14°, then steadily declining again, an effect seen across the entire retreating seasonal cap [Kieffer et al., 2000].

[37] The spectral dominance of the H_2O ice does not mean that H_2O ice dominates by mass: only a small amount of H_2O ice is needed to produce absorptions because of its high absorption coefficients. For example, only 1 mg/cm^2 of water ice (100 μm grain size) overlying CO_2 ice (1 mm grain size) will produce water ice absorptions (Figure 8), or just 0.05 wt% if the two are intimately mixed (Figure 8). Water ice cold trapped onto the surface during winter would

produce weak H_2O absorptions as long as the CO_2 was abundant and coarse grained; however, as the CO_2 sublimates and disintegrates into smaller grains (as seen elsewhere on both polar caps, presumably resulting from an
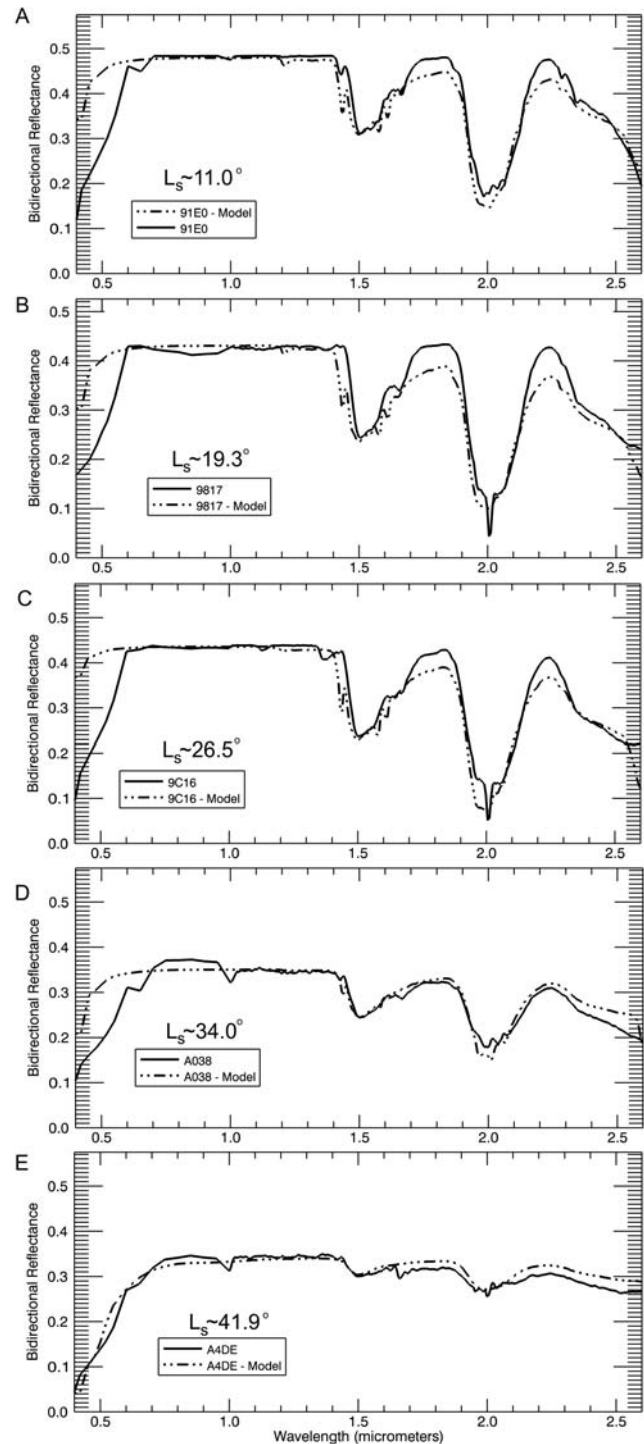

Figure 7. Spring CRISM observations (solid lines) and model results (dotted lines). Water ice dominates spectra in the early spring; however, CO_2 ice-only absorptions are still visible through L_s ~26°. Model parameters for these observations are given in Table 2.
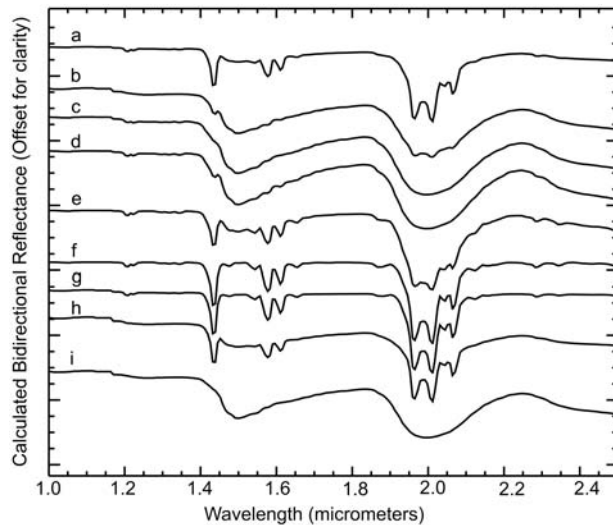
Figure 8. Modeled results of intimate mixtures of CO_2 ice and water ice (Figures 8a and 8b), layers of water ice on top of CO_2 ice (Figures 8c–8e), and layers of CO_2 ice on top of water ice (Figures 8g and 8h). An overlying layer of water ice more than 5 mg/cm^2 thick is sufficient to completely mask CO_2 ice absorptions; however, an overlying layer of CO_2 ice must be thicker than 1000 mg/cm^2 to completely mask water ice absorptions. (a) Intimate mixture of 0.05 wt% water ice (10 μm grain size) + 99.95 wt% CO_2 ice (1 mm grain size). The water ice absorptions are just barely visible. (b) Intimate mixture of 5 wt% water ice (10 μm grain size) + 95 wt% CO_2 ice (1 mm grain size). The CO_2 ice features are almost completely masked. (c) A layer of 10 mg/cm^2 of water ice (10 μm grain size) overlying CO_2 ice (1 mm grain size). The underlying CO_2 is completely masked. (d) A layer of 5 mg/cm^2 of water ice (10 μm grain size) overlying CO_2 ice (1 mm grain size). Some underlying CO_2 ice features are beginning to show up. (e) A layer of 1 mg/cm^2 of water ice (10 μm grain size) overlying CO_2 ice (1 mm grain size). CO_2 ice dominates, with small water ice absorptions. (f) Pure CO_2 ice (1 mm). (g) A layer of 5000 mg/cm^2 CO_2 (1 mm) overlying 10 μm ice, the water absorptions are almost entirely hidden. (h) A layer of 500 mg/cm^2 CO_2 (1 mm) overlying 10 μm ice, the water ice absorptions are pronounced. (i) Pure 10 μm water ice.

increase in solar insulation) [e.g., *Titus et al.*, 2001], the same amount of water ice will dominate the spectrum.

[38] The early spring observations are initially well fit by an intimate mixture of ~0.1 wt% water ice (100 μm grain size), 0.003 wt% soil (3 μm grain size), and slab CO_2 ice (~20 cm path lengths), overlying a layer of soil with grain sizes of ~2 mm (Figure 7a). The ratios and grain sizes of the water ice and soil remain fairly constant throughout the spring; however, the grain sizes of the CO_2 ice layer gradually decreases as the CO_2 ice sublimates (Table 2).

[39] As the CO_2 ice disappeared, the H_2O ice also sublimated, contributing to the midspring hazes observed in HiRISE and CRISM observations during this time. CO_2 ice absorptions disappear from DISORT-corrected FRTs at L_s ~26°; however, features continue to show up in ratioed spectra until L_s ~34°. After L_s ~26°, water ice is completely dominating the spectrum and masking the small CO_2 ice features that remain. This is consistent with *Kieffer and Titus*'s [2001] estimate that the "crocus date" (disappearance of CO_2 frost) at 68°N should be between L_s ~29° and L_s ~48°. The water ice finally disappears around L_s ~59°.

3.4. Sensitivity Analysis Results

[40] A representative sensitivity analysis for a summer ice-free spectrum is shown in Figures 9a and 9b. Component grain sizes are well constrained on the lower end, but poorly constrained on the higher end. The thickness of the top layer is likewise well constrained on the lower end, but less well constrained on the upper end.

[41] Sensitivity analysis was not performed on the winter spectrum, since conclusions about grain sizes were based on absorption bands depths, instead of on the mixing model. A representative sensitivity analysis for spring is shown in Figures 9c–9f. Grain sizes for H_2O ice and soil are well constrained; however, CO_2 ice "grain size" is poorly constrained on the upper limit. The thickness of the CO_2 slab is likewise well defined (Figure 9f).

4. HiRISE Analysis: Data Set and Methods

[42] The spring defrosting period was also monitored with images from HiRISE [*McEwen et al.*, 2007], which have 0.25 to 1.3 m/pixel size and swath widths of ~6 km. The R (570–830 nm) and BG (<580 nm) filter channels were used to monitor annual changes in surface color and the R channel for ice depth measurements, because it has the widest swath width.

[43] Spring ice depth was calculated by comparing rock "heights" in spring and summer images. Rock shadow

Table 2. Modeling Results for Representative FRTs Covering a Range of L_s Values

|		Upper Layer							Lower Layer						
		H_2O Ice		CO_2 Ice		Soil			H_2O Ice		CO_2 Ice		Soil		
L_s	FRT	wt %	cm	wt %	cm	wt %	cm	Thickness (cm)	wt %	cm	wt %	cm	wt %	cm	X2
11	91E0	0.1	0.01	99.897	20	0.003	0.0003	20.17	-	-	-	-	1	0.2	0.333
19.3	9817	0.15	0.02	99.847	20	0.003	0.0003	19.65	-	-	-	-	1	0.2	0.647
26.5	9C16	0.35	0.02	99.647	5.9	0.003	0.0003	9.17	-	-	-	-	1	0.2	0.381
34	A038	0.4	0.015	99.59	4	0.01	0.0003	3.93	-	-	-	-	1	0.2	0.214
41.9	A4DE	35	0.01	-	-	65	0.0003	0.012	-	-	-	-	1	0.2	0.174
156.8	3957	-	-	-	-	100	0.0015	0.009	-	-	-	-	1	0.2	0.106
167.2	3EAD	50	0.005	-	-	50	0.0015	0.0095	-	-	-	-	1	0.2	0.354
176.8	419C	50	0.007	-	-	50	0.0015	0.0113	-	-	-	-	1	0.2	0.041
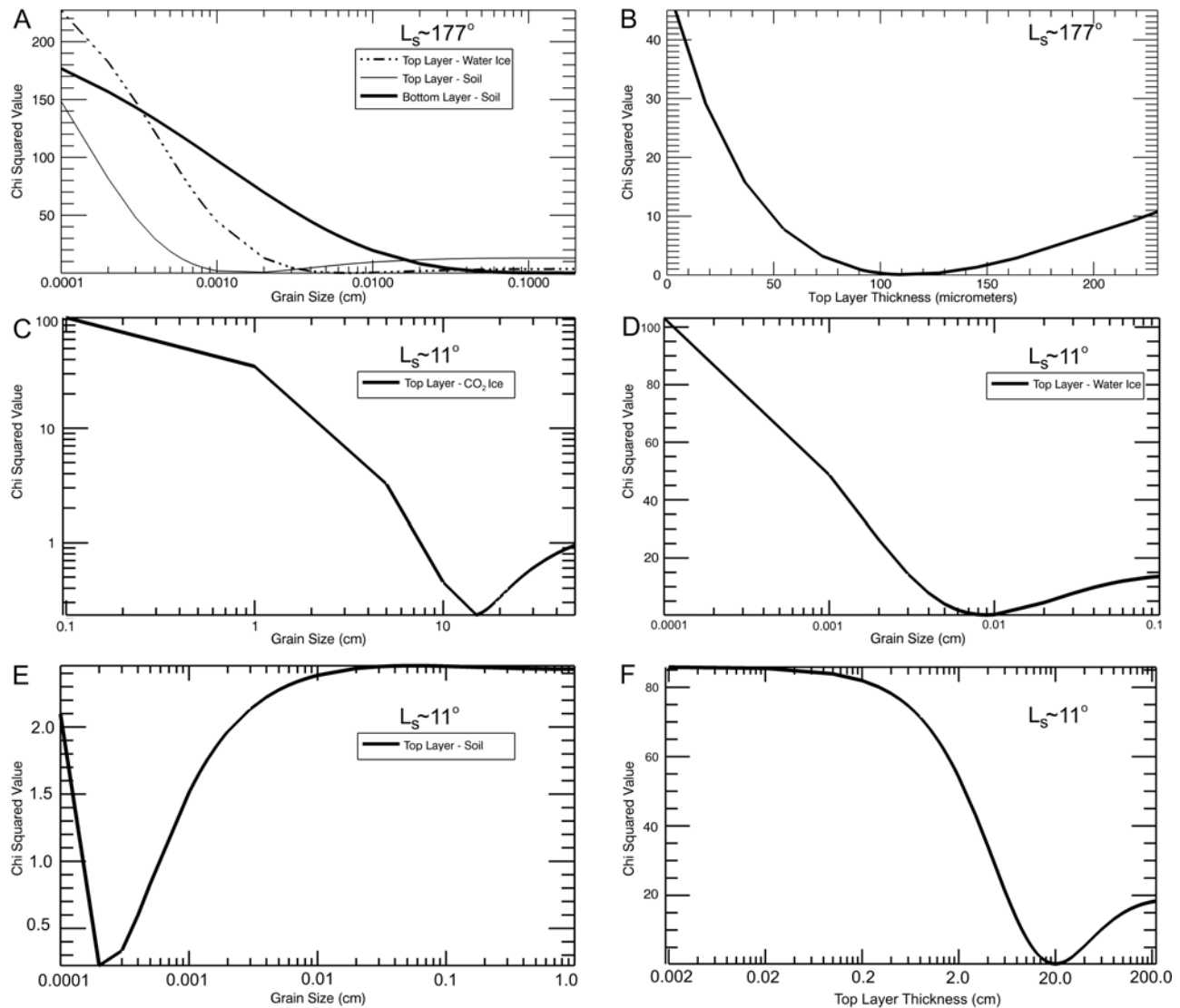
Figure 9. Example of a sensitivity analysis for (a–b) L_s ~177° observation and (c–f) for L_s ~ 11° observation.

lengths in summer HiRISE images were measured parallel to solar azimuth direction, and, with the incidence angles from the HiRISE geometry files, the height of the rock was calculated. The shadow lengths of the same rocks were measured in spring, and, with the new incidence angles, the new rock "heights" were calculated. The difference in summer and spring rock "heights" gives the ice depth, assuming that there was not significant ice on top of the rocks (Figures 10a and 10b). This is a valid assumption, because fine-scale morphology is visible on the tops of large rocks in both summer and spring (Figures 10e and 10f), demonstrating that the tops are relatively uncovered.

[44] It is possible that the high thermal inertia of the rocks also retards ice formation around them. For example, *Sizemore and Mellon* [2006] showed that a rock's influence on the ice table extends ~1–2 rock radii, which is greater than the area usually covered by a rock shadow at typical HiRISE incidence angles. Rocks in many spring HiRISE images often have dark halos around them (e.g., Figure 10f)

because of this effect. An ice-free moat around a rock would make the measured shadows longer (Figure 10d), reducing the inferred depth of ice. Likewise, any ice on top of rocks would make them appear "taller" than they actually are (Figure 10c), reducing the inferred depth of ice. The shadow measurements therefore indicate minimum ice depths.

5. HiRISE Results

5.1. Ice Depth

[45] During winter, few HiRISE images were obtained near the landing site, due to the presence of the polar hood. The few that were obtained showed few rocks due to the thick layer of ice on the ground.

[46] By L_s ~ 3°, the ice layer had become thin enough to expose large rocks, and shadow measurements indicated an ice depth of 34 ± 1 cm. The ice layer continued to thin through spring, reaching 5 ± 1 cm by L_s ~37°. The ice depth
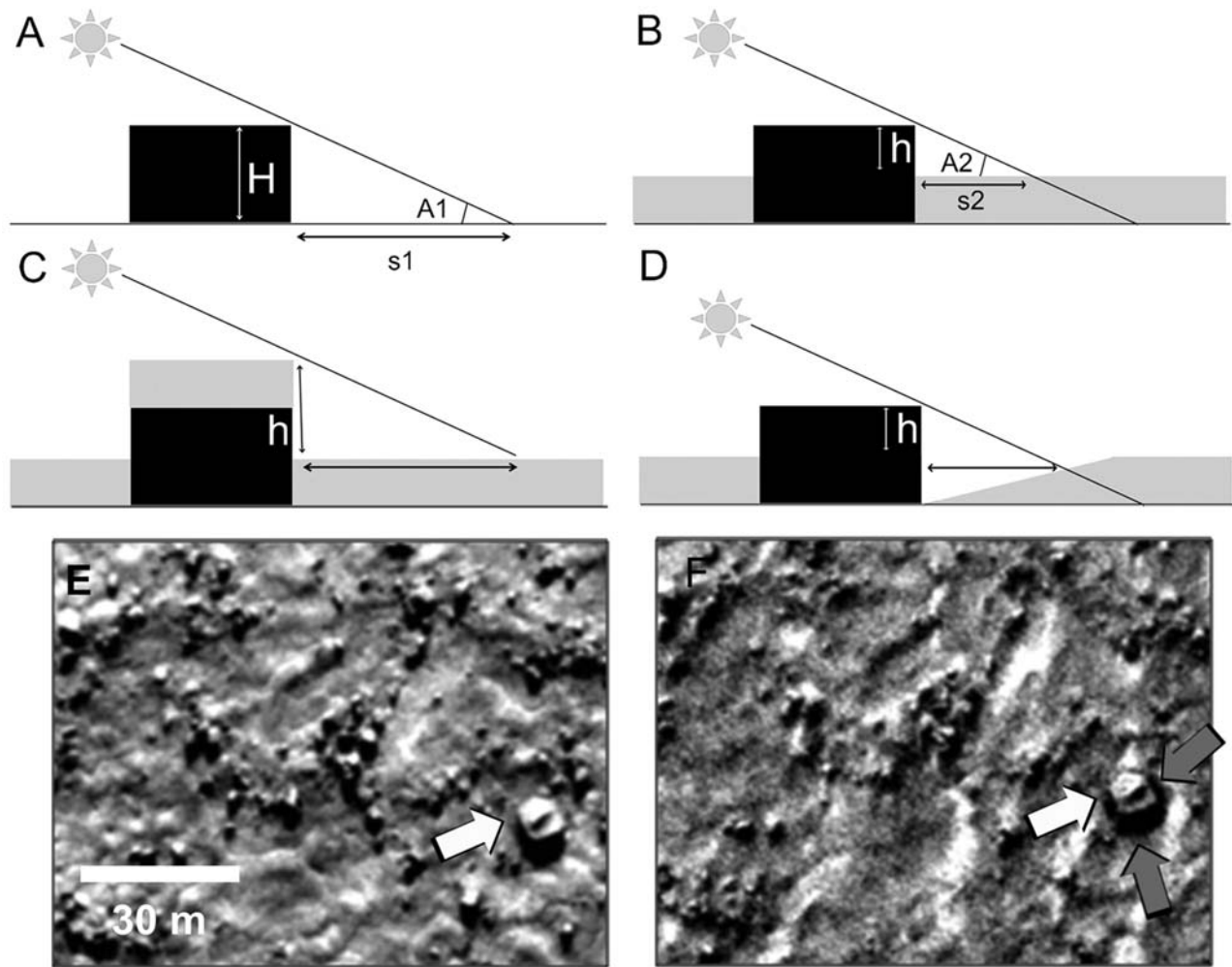
Figure 10. (a) Using rocks as "snowpoles" to measure the depth of snow, we can determine the snow-free height of a rock using shadow lengths, then compare that to the "height" of the rock when the ground is covered with ice, and derive the depth of the snow. The rock shadow length (S1) was measured in summer, and the rock height estimated as H = tan(A1)*S1. (b) The difference in heights between spring and summer was taken as the ice depth. (c) Ice on top of the rock will make the shadow appear longer than what we would have measured without ice on top. This results in smaller calculated ice depths. (d) A reduced ice "moat" around a rock will make the shadow appear longer than what we would have measured without the moat. This results in smaller calculated ice depths. (e) Subset of summer HiRISE image PSP_002012_2485. (f) Subset of spring HiRISE image PSP_006561_2485, showing same scene. Rock marked with a white arrow shows surface morphology not obscured by ice. Gray arrows point to dark halo, which might indicate a reduced ice moat around the rock.

measurements obtained from HiRISE images are listed in Table 3.

5.2. Ice Sublimation Patterns

[47] Our combined HiRISE and CRISM results show that ice does not sublimate uniformly from the Phoenix landing site region. Different sublimation rates are most noticeable over the polygonal terrain that covers this region. At the Phoenix landing site, polygons are usually small (3–6 m across) with troughs ~10 cm deep [*Mellon et al.*, 2008b]. HiRISE and CRISM observations during spring show that high-albedo ice begins disappearing from polygon centers as early as L_s ~18°, and lingers in polygon troughs as late as

L_s ~45° (Figure 11). A similar phenomenon is also observed in the retreat of the southern seasonal cap [*Kossacki and Markiewicz,* 2002; *Kossacki et al.*, 2003].

[48] It is possible that ice is being redistributed to polygon troughs, perhaps by wind. Another possibility is that the ice lingers in the troughs because of thermal inertia effects. Rock-free soil, which is prevalent in the troughs, has a low thermal conductivity (which dominates thermal inertia), meaning that a thick surface soil layer should conduct less summer heat into the subsurface than a denser surface. With less stored heat, the surface will cool faster in the fall and winter, allowing more ice to accumulate. If significant amounts of soil are trapped in polygon troughs by wind, the

Table 3. Ice Depths Derived From HiRISE Measurements for a Range of L_s Values

Ls of Icy Frame	Average Depth (cm)	SD	Ice-Free HiRISE Frame	Icy HiRISE Frame
3	33.6	1.0	PSP_001906_2485	PSP_006495_2485
5	31.4	1.6	PSP_002012_2485	PSP_006561_2485
11	21.1	0.7	PSP_001893_2485	PSP_006706_2485
19	21.8	1.0	PSP_001880_2485	PSP_006917_2485
24	10.6	1.5	PSP_001893_2485	PSP_007062_2485
29	8.3	1.1	PSP_001893_2485	PSP_007207_2485
37	5.0	1.0	PSP_001893_2485	PSP_007418_2485
334	67.3	2.1	PSP_001893_2485	PSP_005783_2485

cooler surface would encourage CO_2 ice formation during fall and retard its sublimation in spring. A similar effect might be expected for the diurnal temperature cycle, as the troughs cool down faster at night. Trough shadowing might also play a role in retaining ice in troughs longer.

[49] In addition to the polygons, defrosting rates differ among the geologic units that were described by *Seelos et al.* [2008]. Lowland dark and knobby terrains lose ices first, followed by block mesa terrain, then highland unit, then lowland bright unit, and finally debris aprons surrounding plateaus (Figure 12). This probably results from higher thermal inertia surfaces that conduct more summer heat into the ground and release it slowly during winter and spring, raising annual mean surface temperatures, retarding ice formation, and speeding ice sublimation. Indeed, in THEMIS predawn thermal IR images, the units that appear brightest (indicating high thermal inertias) are lowland dark and knobby terrain, which lose their ice first.

6. Discussion: Annual Evolution of Ices

[50] In CRISM spectra, water ice first appears at L_s ~167°. The late summer ice is best modeled as 50 μm diameter ice grains, and the presence of a 1.5 μm band makes it unlikely that these are atmospheric ice particles.

[51] Late summer and early fall spectra lack evidence of CO_2 ice (L_s ~142°–181°). It is possible that CO_2 ice is present and masked by the strong H_2O ice absorptions (the H_2O-CO_2 ice modeling shows that 10-μm grain size water ice can hide up to 80 wt% CO_2 in intimate mixture); however, this probably is not happening in early fall, as temperatures are still above the CO_2 condensation temperature of ~140 K [*Kelly et al.*, 2006].

[52] These results are consistent with a number of other observations. The late summer onset of ice is consistent with TES temperature observations, which show that 68°N reaches water condensation temperatures (<190 K) at L_s ~164° [*Kieffer and Titus*, 2001]. Additionally, the amount of water ice accumulating during this period is within the range of perceptible water vapor measured in this area during late summer [e.g., *Houben et al.*, 1997].

[53] By winter, CRISM observations and modeling show a ~30 cm layer of CO_2 ice on the surface. Because of the deep ice-only absorptions seen in this spectrum, the CO_2 must have "grain sizes" on the order of 20 cm, indicating that this material is probably slab ice. The depth of the 1.5 μm band and the shape of the CRISM spectrum between
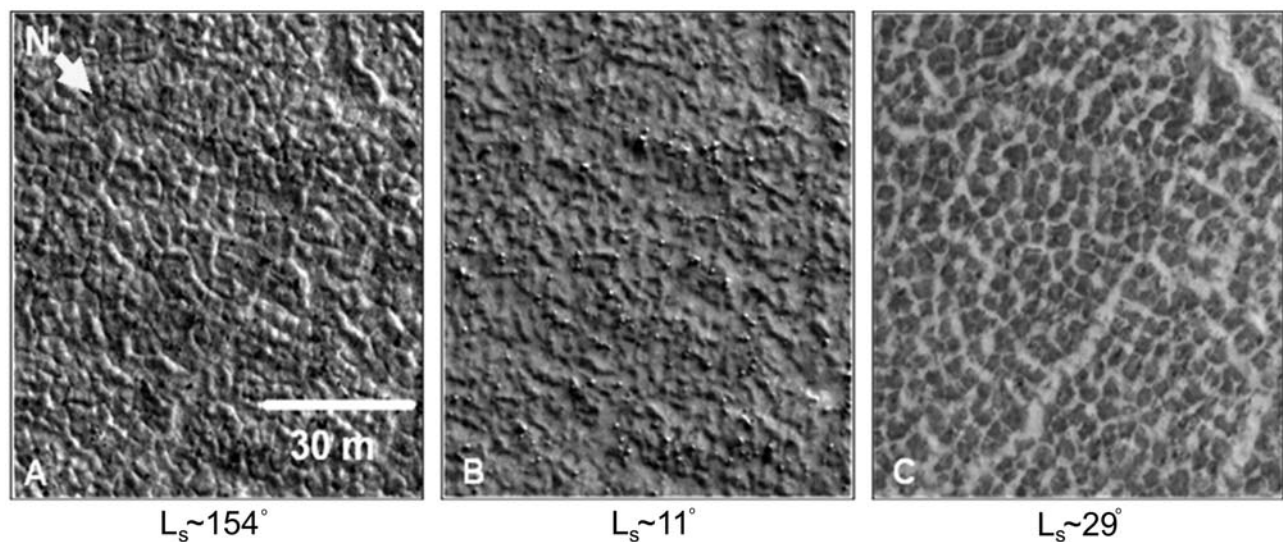

Figure 11. Subsets of HiRISE images illustrating frost coverage through time. (left) During the summer (L_s ~154°), the surface is ice-free. (middle) In early spring (L_s ~11°), the surface is completely covered with ice. (right) By midspring (L_s ~29°), ice has disappeared from the centers of polygons and is lingering in the polygon troughs.
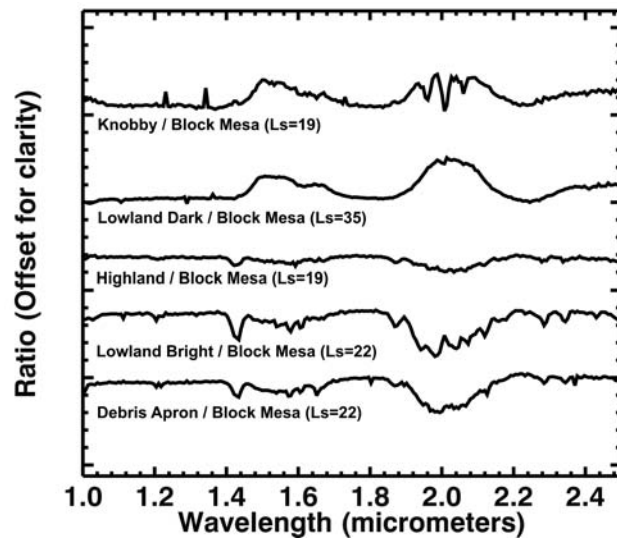
Figure 12. Defrosting patterns for different geomorphic units based on geomorphic units mapped by K. Seelos (personal communication, 2008). The spectra are ratios of different units. The highland, lowland bright, and debris aprons all have deeper CO_2 absorptions than the block mesa unit. Block mesa has deeper ice absorptions than both the lowland dark and knobby terrains. By ratioing to the block mesa unit, we can contrast relative amount and retention of ices. Knobby and lowland dark materials lose both CO_2 and water ice before the block mesa, as evidenced by the inverted shapes in the ratio. Highland, lowland bright, and debris aprons preserve ices longer than block mesa, as the ratios show typical ice features. From bottom to top, these ratios were made with CRISM observations FRT0000999F, FRT0000999F, FRT00009817, FRT0000A0C4, and FRT00009817.

2.2 and 2.5 μm also indicate that some coarse-grained water ice is overlying the slab. The presence of water ice on top of the CO_2 slab indicates that the CO_2 slab is no longer growing at L_s ~344°.

[54] The ~30 cm slab thickness is consistent with thermal models, which predict that at L_s ~340°, the surface should be covered with 170–350 kg/m^2 CO_2, depending on the depth of ground ice [Mellon et al., 2008a]. Assuming a CO_2 ice solid density of 1590 kg/m^3 and a low porosity (30%), this translates to ~16–33 cm of CO_2 ice.

[55] The long path lengths suggest that the ice is in slab form, which is consistent with a number of other observations. Based on physical models, CO_2 ice of any grain size is expected to quickly metamorphose into slab ice in the seasonal deposits [Eluszkiewicz, 1993]. CO_2 slab ice has been invoked to explain a number of polar observations, including low-albedo, cold surfaces [e.g., Kieffer et al., 2000; Titus et al., 2001]. Additionally, Mars Global Surveyor gravity and topography data suggest a seasonal cap mean density close to ~910 kg/m^3, which corresponds to a porosity of only ~40% [Smith et al., 2001], compared to ~70% porosity expected of freshly fallen snow [Eluszkiewicz et al., 2005].

[56] If the CO_2 is in slab ice form, it might be possible to see through the ice to the underlying soil and fall-deposited

water ice. Our modeling shows that a 30 cm thick slab of perfectly pure CO_2 ice (i.e., with no internal scattering surfaces like soil or crystal faces) is transparent at wavelengths <1.5 μm and in the 2.3 to 2.5 μm region. However, a transparent slab of CO_2 ice covering fall-deposited water ice and soil is a poor match for the CRISM winter observation, since it mutes the depth of the 1.5 μm absorption and the slope of the 2.2–2.5 μm region (Figure 13).

[57] After the spring equinox, the ice slab is interpreted to break into smaller grains. CRISM observations and models show a steady decrease in the thickness of the CO_2 ice layer from 20 cm to 4 cm from L_s ~11° to 34°. This decrease matches ice depth measurements from HiRISE, which show the ice layer ~21 cm deep at L_s ~11° to ~5 cm deep at L_s ~47°. The agreement between the ice layer thicknesses produced by the nonlinear mixing model and ice layer thicknesses measured by from HiRISE images is good (Tables 2 and 3).

[58] The different rates of sublimation observed for polygon troughs and centers and for different geomorphic units may be responsible for the widely varying estimates for "crocus dates" from various data sets. Depending on the spatial resolution of the data set, and the criteria each is using to distinguish an ice-free surface (e.g., visual images, surface temperature, spectral properties), the seasonal cap may appear to be "gone" at different times.

7. Summary

[59] This study analyzed CRISM spectra and HiRISE images taken over the Phoenix landing site from summer to early fall (L_s ~142°–181°) and late winter to midspring (L_s ~344°–75°) for the year prior to Phoenix landing. Spectra were atmospherically corrected using the DISORT radiative transfer method, and compared to nonlinear mixing models of soil-H_2O-CO_2 mixtures. Matching summer/spring pairs of HiRISE images were used to calculate ice depths based on changes in rock shadow length. This study draws the following conclusions about seasonal ice at the Phoenix landing site:

[60] 1. Water ice precedes CO_2 ice during the onset of the seasonal cap. Water ice first appears on the surface at L_s ~167°. CO_2 ice begins to condense at L_s > 181°.
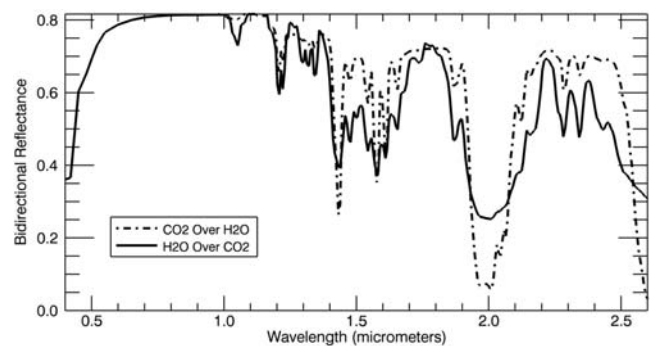

Figure 13. Models comparing a CO_2 ice slab over water ice to a water ice layer over CO_2. The CO_2 covering water ice almost entirely masks the H_2O underneath; however, a thin layer of water ice over CO_2 allows CO_2 absorptions to show.

[61] 2. During winter, the seasonal cap at the Phoenix landing site consists of a ~30 cm thick layer of nearly pure CO_2 ice, probably in the form of slab ice. A thin layer ~100 μm water ice overlies the CO_2 slab. The surface appears slightly red during winter from the soil contamination; however, we are not seeing through the ice to the underlying surface.

[62] 3. During spring, the CO_2 ice deteriorates into smaller grain sizes and sublimates, producing spectra that are increasingly dominated by water ice. Our modeling supports the hypothesis that the spring water ice annulus is due to water ice cold trapped onto the surface of the CO_2 ice, not due to an underlying layer of water ice that is exposed during CO_2 sublimation.

[63] 4. CO_2 ice finally disappears after L_s ~34°. The water ice finally disappears around L_s ~59°.

[64] 5. Ice sublimation is not uniform: it disappears first from polygon centers, and only later from troughs. This probably results from soil trapped in polygon troughs, lowering the thermal inertia and surface temperature, or due to redistribution by wind.

[65] 6. Ice sublimation also varies among geomorphic units. In the region D geomorphic units defined by *Seelos et al.* [2008], ice disappears first from the lowland dark and knobby units, then block mesa, then highland, then lowland bright, and finally from debris aprons. This pattern also likely results from thermal inertia differences.

References

Aharonson, O. (2004), Sublimation at the base of a seasonal CO_2 slab on Mars, *Lunar Planet. Sci.*, *XXXV*, Abstract 1918.

Arvidson, R. E., J. L. Gooding, and H. J. Moore (1989), The Martian surface as imaged, sampled, and analyzed by the Viking Landers, *Rev. Geophys.*, *27*(1), 39–60, doi:10.1029/RG027i001p00039.

Arvidson, R. E., et al. (2008), Mars Exploration Program 2007 Phoenix landing site selection and characteristics, *J. Geophys. Res.*, *113*, E00A03, doi:10.1029/2007JE003021.

Arvidson, R. E., et al. (2009), Results from the Mars Phoenix Lander Robotic Arm experiment, *J. Geophys. Res.*, *114*, E00E02, doi:10.1029/2009JE003408.

Benson, J. L., and P. B. James (2005), Yearly comparisons of the Martian polar caps: 1999–2003 Mars Orbiter Camera observations, *Icarus*, *174*, 513–523, doi:10.1016/j.icarus.2004.08.025.

Bibring, J.-P., et al. (2005), Mars surface diversity as revealed by OMEGA/Mars Express observations, *Science*, *307*, 1576, doi:10.1126/science.1108806.

Byrne, S., et al. (2008), Interannual and seasonal behavior of Martian residual ice-cap albedo, *Planet. Space Sci.*, *56*(2), 194–211, doi:10.1016/j.pss.2006.03.018.

Clancy, R. T., S. W. Lee, G. R. Gladstone, W. W. McMillan, and T. Rousch (1995), A new model for Mars atmospheric dust based upon analysis of ultraviolet through infrared observations from Mariner 9, Viking, and Phobos, *J. Geophys. Res.*, *100*(E3), 5251–5263, doi:10.1029/94JE01885.

Clancy, R. T., M. J. Wolff, and P. R. Christensen (2003), Mars aerosol studies with the MGS TES emission phase function observations: Optical depths, particle sizes, and ice cloud types versus latitude and solar longitude, *J. Geophys. Res.*, *108*(E9), 5098, doi:10.1029/2003JE002058.

Conrath, B. J., J. C. Pearl, M. D. Smith, W. C. Maguire, P. R. Christensen, S. Dason, and M. S. Kaelberer (2000), Mars Global Surveyor Thermal

Emission Spectrometer (TES) observations: Atmospheric temperatures during aerobraking and science phasing, *J. Geophys. Res.*, *105*(E4), 9509–9519, doi:10.1029/1999JE001095.

Cull, S. C., et al. (2010), The seasonal ice cycle at the Mars Phoenix landing site: 2. Postlanding CRISM and ground observations, *J. Geophys. Res.*, doi:10.1029/2009JE003410, in press.

Domingue, D., B. Hartman, and A. Verbiscer (1997), The scattering properties of natural terrestrial snows versus icy satellite surfaces, *Icarus*, *128*, 28–48, doi:10.1006/icar.1997.5733.

Eluszkiewicz, J. (1993), On the microphysical state of the Martian polar caps, *Icarus*, *103*, 43–48, doi:10.1006/icar.1993.1056.

Eluszkiewicz, J., J.-L. Moncet, T. N. Titus, and G. B. Hansen (2005), A microphysically based approach to modeling emissivity and albedo of the Martian seasonal caps, *Icarus*, *174*, 524–534, doi:10.1016/j.icarus.2004.05.025.

Forget, F., G. B. Hansen, and J. B. Pollack (1995), Low brightness temperatures of Martian polar caps: CO_2 clouds or low surface emissivity?, *J. Geophys. Res.*, *100*(E10), 21,219–21,234, doi:10.1029/95JE02378.

Forget, F., F. Hourdin, and O. Talagrand (1998), CO_2 snowfall on Mars: Simulation with a general circulation model, *Icarus*, *131*, 302–316, doi:10.1006/icar.1997.5874.

Haberle, R. M., et al. (2008), The effect of ground ice on the Martian seasonal CO_2 cycle, *Planet. Space Sci.*, *56*, 251–255, doi:10.1016/j.pss.2007.08.006.

Hansen, G. B. (1997), The infrared absorption spectrum of carbon dioxide ice from 1.8 to 333 μm, *J. Geophys. Res.*, *102*, 21,569–21,587, doi:10.1029/97JE01875.

Hansen, G. B. (2005), Ultraviolet to near-infrared absorption spectrum of carbon dioxide ice from 0.174 to 1.8 μm, *J. Geophys. Res.*, *110*, E11003, doi:10.1029/2005JE002531.

Hapke, B. (1981), Bidirectional reflectance spectroscopy: 1. Theory, *J. Geophys. Res.*, *86*(B4), 3039–3054, doi:10.1029/JB086iB04p03039.

Hapke, B. (1984), Bidirectional reflectance spectroscopy: 3. Correction for macroscopic roughness, *Icarus*, *59*, 41–59, doi:10.1016/0019-1035(84)90054-X.

Hapke, B. (1993), *Theory of Reflectance and Emittance Spectroscopy*, Cambridge Univ. Press, Cambridge, U. K.

Heet, T., et al. (2009), Geomorphic and geologic settings of the Phoenix lander mission landing site, *J. Geophys. Res.*, *114*, E00E04, doi:10.1029/2009JE003416.

Henyey, L. G., and J. L. Greenstein (1941), Diffuse radiation in the galaxy, *Astrophys. J.*, *93*, 70–83, doi:10.1086/144246.

Houben, H., et al. (1997), Evolution of the Martian water cycle, *Adv. Space Res.*, *19*(8), 1233–1236, doi:10.1016/S0273-1177(97)00274-3.

James, P. B., and B. A. Cantor (2001), Martian north polar cap recession: 2000 Mars Orbiter Camera observations, *Icarus*, *154*, 131–144, doi:10.1006/icar.2001.6653.

James, P. B., et al. (1993), The seasonal cycle of carbon dioxide on Mars, in *Mars*, edited by H. Kieffer, pp. 934–968, Univ. of Ariz. Press, Tucson.

Johnson, J. R., et al. (1999), Preliminary results on photometric properties of materials at the Sagan Memorial Station, Mars, *J. Geophys. Res.*, *104*(E4), 8809–8830, doi:10.1029/98JE02247.

Johnson, J. R., et al. (2006), Spectrophotometric properties of materials observed by Pancam on the Mars Exploration Rovers: 1. Spirit, *J. Geophys. Res.*, *111*, E02S14, doi:10.1029/2005JE002494.

Jouglet, D., F. Poulet, R. E. Milliken, J. F. Mustard, J.-P. Bibring, Y. Langevin, B. Gondet, and C. Gomez (2007), Hydration state of the Martian surface as seen by Mars Express OMEGA: 1. Analysis of the 3 μm hydration feature, *J. Geophys. Res.*, *112*, E08S06, doi:10.1029/2006JE002846.

Kelly, N. J., W. V. Boynton, K. Kerry, D. Hamara, D. Janes, R. C. Reedy, K. J. Kim, and R. M. Haberle (2006), Seasonal polar carbon dioxide frost on Mars: CO_2 mass and columnar thickness distribution, *J. Geophys. Res.*, *111*, E03S07, doi:10.1029/2006JE002678.

Kieffer, H. H. (2007), Cold jets in the Martian polar caps, *J. Geophys. Res.*, *112*, E08005, doi:10.1029/2006JE002816.

Kieffer, H. H., and T. N. Titus (2001), TES mapping of Mars' northern seasonal cap, *Icarus*, *154*, 162–180, doi:10.1006/icar.2001.6670.

Kieffer, H. H., T. N. Titus, K. F. Mullins, and P. R. Christensen (2000), Mars south polar spring and summer behavior observed by TES: Seasonal cap evolution controlled by frost grain size, *J. Geophys. Res.*, *105*(E4), 9653–9699, doi:10.1029/1999JE001136.

Kirk, R. L., et al. (2008), Ultrahigh resolution topographic mapping of Mars with MRO HiRISE stereo images: Meter-scale slopes of candidate Phoenix landing sites, *J. Geophys. Res.*, *113*, E00A24, doi:10.1029/2007JE003000.

Kossacki, K. J., and W. J. Markiewicz (2002), Martian seasonal CO_2 ice in polygonal troughs in southern polar region: Role of the distribution of subsurface H_2O ice, *Icarus*, *160*, 73–85, doi:10.1006/icar.2002.6936.

Kossacki, K. J., et al. (2003), Surface temperature of Martian regolith with polygonal features: Influence of the subsurface water ice, *Planet. Space Sci.*, *51*, 569–580, doi:10.1016/S0032-0633(03)00070-9.

Larson, H. P., and U. Fink (1972), Identification of carbon dioxide frost on the Martian polar caps, *Astrophys. J.*, *171*, L91–L95, doi:10.1086/180875.

Litvak, M. L., et al. (2005), Modeling of Martian seasonal caps from HEND/ODYSSEY data, *Adv. Space Res.*, *36*, 2156–2161, doi:10.1016/j.asr.2005.09.007.

McEwen, A. S., et al. (2007), Mars Reconnaissance Orbiter's High Resolution Imaging Science Experiment (HiRISE), *J. Geophys. Res.*, *112*, E05S02, doi:10.1029/2005JE002605.

Mellon, M. T., W. V. Boynton, W. C. Feldman, R. E. Arvidson, T. N. Titus, J. L. Bandfield, N. E. Putzig, and H. G. Sizemore (2008a), A prelanding assessment of the ice table depth and ground ice characteristics in Martian permafrost at the Phoenix landing site, *J. Geophys. Res.*, *113*, E00A25, doi:10.1029/2007JE003067.

Mellon, M. T., R. E. Arvidson, J. J. Marlow, R. J. Phillips, and E. Asphaug (2008b), Periglacial landforms at the Phoenix landing site and the northern plains of Mars, *J. Geophys. Res.*, *113*, E00A23, doi:10.1029/2007JE003039.

Milliken, R. E., J. F. Mustard, F. Poulet, D. Jouglet, J.-P. Bibring, B. Gondet, and Y. Langevin (2007), Hydration state of the Martian surface as seen by Mars Express OMEGA: 2. H_2O content of the surface, *J. Geophys. Res.*, *112*, E08S07, doi:10.1029/2006JE002853.

Murchie, S., et al. (2007), Compact Reconnaissance Imaging Spectrometer for Mars (CRISM) on Mars Reconnaissance Orbiter (MRO), *J. Geophys. Res.*, *112*, E05S03, doi:10.1029/2006JE002682.

Pike, W.T., et al. (2009), Fractal analysis of the microstructure of the Martian soil at the Phoenix landing site, *Lunar Planet. Sci.*, *XL*, Abstract 1909.

Roush, T. L. (1994), Charon: More than water ice?, *Icarus*, *108*, 243–254, doi:10.1006/icar.1994.1059.

Seelos, K. D., et al. (2008), Geomorphologic and mineralogic characterization of the northern plains of Mars at the Phoenix Mission candidate landing sites, *J. Geophys. Res.*, *113*, E00A13, doi:10.1029/2008JE003088.

Sizemore, H. G., and M. T. Mellon (2006), Effects of soil heterogeneity on Martian ground-ice stability and orbital estimates of ice table depth, *Icarus*, *185*, 358–369, doi:10.1016/j.icarus.2006.07.018.

Smith, D. E., et al. (2001), Seasonal variations of snow depth on Mars, *Science*, *294*, 2141–2146, doi:10.1126/science.1066556.

Smith, M. D. (2002), The annual cycle of water vapor on Mars as observed by the Thermal Emission Spectrometer, *J. Geophys. Res.*, *107*(E11), 5115, doi:10.1029/2001JE001522.

Smith, M. D. (2004), Interannual variability in TES atmospheric observations of Mars during 1999–2003, *Icarus*, *167*, 148–165, doi:10.1016/j.icarus.2003.09.010.

Smith, P. H., et al. (2008), Introduction to special section on the Phoenix Mission: Landing site characterization experiments, mission overviews, and expected science, *J. Geophys. Res.*, *113*, E00A18, doi:10.1029/2008JE003083.

Smith, P. H., et al. (2009), Water at the Phoenix landing site, *Science*, *325*, 58–61.

Stamnes, K., et al. (1988), Numerically stable algorithm for discrete-ordinate-method radiative transfer in multiple-scattering and emitting layered media, *Appl. Opt.*, *27*, 2502–2509, doi:10.1364/AO.27.002502.

Titus, T. N., H. H. Kieffer, K. F. Mullins, and P. R. Christensen (2001), TES premapping data: Slab ice and snow flurries in the Martian north polar night, *J. Geophys. Res.*, *106*(E10), 23,181–23,196, doi:10.1029/2000JE001284.

Wagstaff, K. L., et al. (2008), Observations of the north polar water ice annulus on Mars using THEMIS, *Planet. Space Sci.*, *56*, 256–265, doi:10.1016/j.pss.2007.08.008.

Warren, S. G. (1984), Optical constants of ice from the ultraviolet to the microwave, *Appl. Opt.*, *23*, 1206–1225, doi:10.1364/AO.23.001206.

Wiseman, S., et al. (2007), Initial analysis of CRISM data over Meridiani Planum, *Lunar Planet. Sci.*, *XXXVIII*, Abstract 1945.

Wiseman, S. (2009), Spectral and stratigraphic mapping of hydrated sulfate and phyllosilicate-bearing deposits: Implications for the aqueous history of Sinus Meridiani, Mars, Ph.D. dissertation, 178 pp., Washington Univ. in St. Louis, St. Louis, Mo.

Wolff, M. J., et al. (2007), Some studies of Martian aerosol properties using MRO/CRISM and MRO/Marci, in *Seventh International Conference on Mars, July 9–13, 2007, Pasadena CA* [CD-ROM], *LPI Contrib.*, *1353*, Abstract 3121.

Wolff, M. J., M. D. Smith, R. T. Clancy, R. Arvidson, M. Kahre, F. Seelos IV, S. Murchie, and H. Savijärvi (2009), Wavelength dependence of dust aerosol single scattering albedo as observed by the Compact Reconnaissance Imaging Spectrometer, *J. Geophys. Res.*, *114*, E00D04, doi:10.1029/2009JE003350.

R. E. Arvidson, S. Cull, and S. Wiseman, Department of Earth and Planetary Sciences, Washington University in Saint Louis, Saint Louis, MO 63112, USA.

R. Clark, U.S. Geological Survey, Box 25046, Denver Federal Center, Denver, CO 80225, USA.

P. McGuire, Institute for Geosciences, Freie Universitaet Berlin, D-12249 Berlin, Germany.

M. Mellon, Laboratory for Atmospheric and Space Physics, University of Colorado at Boulder, Boulder, CO 80309, USA.

R. V. Morris, ARES, NASA Johnson Space Center, Houston, TX 77058, USA.

T. Titus, U.S. Geological Survey, 2255 N. Gemini Dr., Flagstaff, AZ 86001, USA.